On the use of the profiled singular-function expansion in gravity gradiometry

De Villiers, Geoffrey; Ridley, Kevin; Rodgers, Anthony; Boddice, Daniel

DOI:
10.1016/j.jappgeo.2019.103830

Document Version
Peer reviewed version

Citation for published version (Harvard):
De Villiers, G, Ridley, K, Rodgers, A & Boddice, D 2019, 'On the use of the profiled singular-function expansion in gravity gradiometry', *Journal of Applied Geophysics*, vol. 170, 103830.
https://doi.org/10.1016/j.jappgeo.2019.103830

On the use of the profiled singular-function expansion in gravity gradiometry

G. D. de Villiers, K. D. Ridley and A.D. Rodgers,

UK National Quantum Technology Hub for Sensors and Metrology,

School of Physics and Astronomy,

University of Birmingham, UK.

D. Boddice,

School of Engineering,

University of Birmingham, UK.

Abstract

We demonstrate a method of inverting gravity data, based on profiled singular-function expansions. It is well known that the inverse problem of determining underground density variations from gravity data is severely ill-posed and prior knowledge is needed to restrict the range of possible solutions. Viewed as a linear inverse problem, various standard methods, all of which produce solutions approximating the generalised solution, tend to give density variations concentrated near the surface. To overcome this potentially undesirable trait, various authors have introduced depth weighting. In this paper we carry this idea a step further and introduce a method based on a profiled singular-function expansion which uses the prior knowledge that the underground object is centred at a particular depth. The use of an appropriate depth-weighting profile leads to a solution at the correct depth. Furthermore, we show that if the depth of the object is unknown, a range of solutions at different depths can be produced, allowing other prior knowledge, such as object size or density, to be introduced to determine which solution is the most plausible. The truncation point of the profiled singular-function expansion is determined by the level of noise on the data. We examine how the achievable horizontal resolution varies with this truncation point. A notable property of our approach is that when the centre of the profile corresponds to the true object depth, the solution appears, in a certain sense, to be the most focussed one. Finally we consider a gravimetry example using real data.

Keywords

Geophysical signal processing, Gravity gradient measurement, inverse problems.

1. Introduction

A gravity survey will typically measure data at a number of different horizontal positions above the ground surface. These data will be influenced by underground density variations, as well as other effects such as tidal effects, terrain effects and gravimeter drift. The inverse problem comprises using the data to estimate the density variations. In this paper we concentrate on gradiometry, where the data consist of vertical gradients of the vertical component of gravity, but we note that

the same mathematical approach can be used for gravimetry, i.e. when the vertical component of gravity is measured; in fact, we apply our approach to some real gravimetry data in section 9. A possible application would be locating the horizontal position and depth of an artificial structure, such as a drainage pipe or tunnel. A gradiometer has advantages for such an application because it is more sensitive to nearby objects than distant ones; it is much less sensitive to errors in the vertical tilt of the instrument, for example. This is because the ratio of the desired gravity gradient to the Earth's background gravity gradient is much larger than the ratio of the equivalent desired gravitational acceleration to the Earth's gravitational acceleration. A gradiometer is also more practical in terms of noise suppression because common-mode sources of noise such as microseisms cancel out; this means one can take measurements faster and more accurately because of the reduced integration time. Recent developments in cold-atom gravity sensors raise the prospect of highly-sensitive gradiometers based on quantum technology which could be well matched to this type of application (see, for example, Boddice et al., 2017, Hinton et al., 2017, and Sorrentino et al. 2014).

It is well known that gravity inversion does not have a unique solution, i.e. many different mass distributions can give rise to the same data (see, for example, Roy, 1962, and Zhdanov, 2015, page 30). One aspect of this is depth ambiguity: when data are collected above ground for the purpose of extracting information about underground mass distributions, objects at different depths (which differ in form) may produce virtually identical data. The only way to address ambiguity is by using prior knowledge or assumptions (Paoletti et al., 2013). That is, from a range of possible solutions one picks those that agree with what is already known or assumed.

We will see that the method we propose in this paper has some ability to determine the depth of an object, when this depth is well-defined. Therefore it is worth reviewing some of the ways in which depth determination is addressed in the literature. Given an unknown source at a given depth, an early way of estimating the maximum depth of this source was proposed in Smith and Bott (1958) and Smith (1959). This approach relies on the density variation of the source around the background value having a fixed sign. More recent approaches are linked to Euler deconvolution (Reid et al 1990). In this, the field is assumed homogeneous and the structural index is used to aid in interpretation of the data.

Various imaging methods are discussed in Fedi and Pilkington (2012). These methods can be thought of as upward continuation together with an appropriate depth weighting. Amongst these methods the depth from extreme points (DEXP) method (Fedi, 2007) is noteworthy, in that the weighting depends on the structural index arising in Euler deconvolution. Other methods falling into this category are migration methods (Zhdanov, 2002, Zhdanov et al, 2010) and the continuous-wavelet-transform method (Moreau et al, 1997). These methods are not inversion methods, though they could be thought of as giving a starting point for an inversion process (Fedi and Pilkington, 2012).

In contrast to the imaging methods discussed above one can attempt to solve the inverse problem. The drawbacks to this are very well known; the ill-posedness of the inverse problem implies extreme sensitivity to noise and a wide range of solutions, all of which fit the data. In gravity problems we also typically have the problem of the dimension mismatch, where the data space has one fewer dimension than the object space. This makes the inverse problem rather ill-defined, since the solution depends strongly on how one discretises the different dimensions in the object space.

A standard way of attempting to solve a linear inverse problem involves finding the generalised solution. This corresponds to finding, amongst the wide range of possible solutions, the solution with minimum 2-norm. In the case of the gravity inversion the generalised solution is confined to very

shallow depths, since the inverse-distance law of gravity means that solutions with small density values must be concentrated near the surface (see, for example, Fedi and Pilkington, 2012, Barbosa et al., 2002, Silva et al., 2001, or Zhdanov, 2015, page 289). Determining the generalised solution is not, however, a well-posed problem and a way to mitigate the effects of noise on the data is to write the generalised solution in terms of the singular-function expansion and then to truncate the latter, the truncation point being determined by the noise level.

In order to avoid a solution which is concentrated near the surface it is necessary to introduce depth weighting. There are various other ways of introducing depth weighting into the inverse problem (Paoletti et al., 2013). Li and Oldenburg (1996), introduced depth weighting into full 3D inversion of magnetic data and they extended this in Li and Oldenburg (1998), to gravity data. In their work the depth weighting is included by modifying the penalty term in a version of Tikhonov regularisation, in order to penalise solutions concentrated near the surface. This is discussed further in Zhdanov (2015). A range of weightings are also discussed in Boulanger and Chouteau (2001).

Cella and Fedi (2012), show that the depth weighting of Li and Oldenburg can be improved on by choosing a depth weighting determined by the structure index of the object, when this is well-defined.

There are a number of advantages in using the truncated singular-function expansion to solve the inverse problem. It is simple to calculate and gives a good approximation to the generalised solution (Bertero and Boccacci, 1998). One calculates the singular functions in advance and then one just has to perform a few scalar products and divisions to arrive at the solution. It is also easy to take noise on the data into account: noise simply determines the truncation point of the singular-function expansion. In addition, unlike some other methods (e.g. Fourier methods, see, for example, Cribb, 1976 and Fedi and Pilkington, 2012), there is no need for the data to be sampled on a regular grid, so one avoids issues relating to interpolation and resampling. In addition, unlike methods such as the conjugate-gradient method, the SVD approach does not require multiple iterations.

The SVD seems well-suited for small-scale surveys searching for near-surface features. However, if the size of the survey is sufficiently large, the computational cost of calculating the SVD must be taken into account. Under such circumstances the use of Fourier methods may be preferable.

The standard singular-value decomposition (SVD) has been used in 3D gravity inversion by various authors (Fedi and Rapolla, 1999, Fedi et al., 2005, and Paoletti et al., 2014). However, to the best of our knowledge, the use of the profiled SVD to produce solutions at different depths has not been previously reported. The SVD has also been used (Pilkington, 2012) in full tensor gradiometry for analysing the effectiveness of different tensor components in reconstructing the source of an anomaly. This work is taken further in Paoletti et al. (2016). In this paper we restrict ourselves to the z,z component of the gradient tensor, where z is the vertical coordinate.

We investigate the use of the truncated profiled singular-function expansion as a means of addressing the dimension mismatch between the data space and the object space. The profiled singular-value decomposition, or profiled singular-function expansion, is a method for including prior information about the depth of the objects that give rise to gravity anomalies. We note that this method assumes that all objects lie at a similar depth, i.e. one does not have the situation where an object is greatly extended in depth or where one object is directly below another.

For simplicity and ease of presentation we choose primarily to work in 2D, i.e. one horizontal coordinate and one vertical coordinate; however, extension to 3D is straightforward and we give some simulation results to demonstrate this. We note that the 2D formulation to the problem would

be relevant to a survey line over a long pipe, where the scan is known to be perpendicular to the pipe direction and the pipe can be assumed to have an effectively infinite length.

2. Gravity inversion as a linear inverse problem

Inverse problems can be classified as linear or non-linear. An example of a non-linear method in gravimetry would be to assume that the object of interest is a polyhedron of uniform density and then to estimate the positions of its vertices from the data; this type of method requires very strong prior knowledge of the object. This can be done within a Bayesian framework (see, for example, Rossi, 2013, Brown et al., 2016). Linear methods start from a linear relationship between the underlying density variation and the data and they find a solution which depends linearly on the data. The SVD method is one such method.

For simplicity let us start our discussion with a general one-dimensional linear inverse problem specified by a linear integral equation. For a one-dimensional object and one-dimensional continuous data this equation is of the form

$$g(y) = \int_a^b K(y,s) f(s) ds, \qquad c \le y \le d, \tag{1}$$

where *g* represents the data, *K* is the kernel of the integral equation and *f* is the unknown object. For the sake of notational simplicity we write this in operator notation as

$$g = Kf. \tag{2}$$

Here we use the same symbol for the operator *K* in (2) and its kernel in (1).

We will assume that *f* and *g* lie in Hilbert spaces *F* and *G* respectively, henceforth referred to as the object and data spaces. These are typically spaces of functions which are square-integrable in the Lebesgue sense. We denote these by $L^2(a,b)$ or $L^2(c,d)$.

Typically, if the limits of integration *a* and *b* in (1) are finite, the operator *K* in (2) is compact and of infinite rank. The operator *K* then has a singular-value decomposition and the singular values may be ordered so that they decay towards zero with increasing index (Bertero and Boccacci, 1998). This decay of the singular values makes the inverse problem ill-posed, in that small changes in the data, due to the inevitable noise, can give rise to large changes in the reconstructed object. In other words, the inverse operator to *K* is discontinuous. The way to overcome this ill-posedness is usually via regularisation, whereby the discontinuous inverse to *K* is approximated by a continuous operator, the regularisation operator, parameterised by a regularisation parameter. The choice of the latter depends on the noise level in the data and, in the limit as the noise level shrinks to zero, the regularisation parameter also tends to zero and the discontinuous inverse to *K* is retrieved.

If the inverse problem is severely ill-posed (as is the case for compact *K* with infinite rank) then, in the presence of noise, there are effectively an infinite number of solutions. As mentioned previously, the number of such solutions, and hence the ambiguity, then needs to be reduced via the use of prior information.

Now let us focus on the gradiometry problem. The basic equation in two dimensions is

$$g(x',z') = \gamma \int\int K(x',x,z',z) f(x,z) dx dz, \tag{3}$$

where Υ is the gravitational constant, g is the (continuous) data consisting of the vertical gravity gradients, f is the object to be reconstructed and the kernel K is given by Hinze et al. (2013):

$$K(x', x, z', z) = \frac{4(z'-z)^2}{((z'-z)^2 + (x'-x)^2)^2} - \frac{2}{(z'-z)^2 + (x'-x)^2}. \tag{4}$$

The horizontal and depth coordinates are x and z respectively. Here, we assume that the data are corrected for the Earth's background gravitational field and the surface topography. The integral in (3) is taken to be over an area containing the source of the anomaly of interest. If we allow both x' and z' to vary, the resulting inverse problem is then in the form of a two-dimensional equivalent of that specified by (1). Note, however, that we will treat z' as being fixed, so that the data are measured in one horizontal plane.

3. The singular-function expansion

Let us now discuss the use of the standard singular-value decomposition in the gradiometry problem. We start by considering the singular-value decomposition for the general one-dimensional linear inverse problem with continuous data and a compact forward operator K, as in (1). We assume for simplicity that the data and the object are functions of one-dimensional continuous variables. We will then consider the more realistic problem with discrete data and a finely-discretised object.

Associated with the forward operator K in (2) we have an adjoint operator $K^\dagger$ defined by

$$\left\langle g, Kf \right\rangle_G = \left\langle K^\dagger g, f \right\rangle_F \tag{5}$$

where $\langle \cdot, \cdot \rangle_F$ and $\langle \cdot, \cdot \rangle_G$ are the scalar products in the object and data spaces respectively.

The operator K has a singular-value decomposition given by the set of triplets $\{\alpha_i, u_i, v_i\}_{i=0}^{\infty}$, where the α_i are the singular values, the u_i are the right-hand singular functions and the v_i are the left-hand singular functions. These satisfy the coupled equations (Bertero and Boccacci, 1998):

$$Ku_i = \alpha_i v_i \tag{6}$$

and

$$K^\dagger v_i = \alpha_i u_i . \tag{7}$$

The right- and left-hand singular functions form complete orthonormal bases for the ranges of $K^\dagger$ and K respectively. A solution to (1) can then be written in the form

$$\tilde{f}(s) = \sum_{k=0}^{\infty} \frac{b_k}{\alpha_k} u_k(s), \tag{8}$$

where the b_k are given by

$$b_k = \left\langle g, v_k \right\rangle_G . \tag{9}$$

Note that in (8) we have assumed that the range of *K* is infinite-dimensional. The solution in (8) is the generalised solution to (1). Other solutions may be obtained from this by adding elements in the null-space of *K*, if this is non-trivial, since these elements have no effect on the data.

In practice, determination of the generalised solution is still an ill-posed problem since, as the singular values become very small, the expansion coefficients in (8) become very sensitive, via (9), to noise on the data. One way around this is to truncate the expansion:

$$\tilde{f}(s) = \sum_{k=0}^{M} \frac{b_k}{\alpha_k} u_k(s) , \tag{10}$$

where the truncation point *M* depends on the noise level. The resulting approximate solution is then called the truncated singular-function expansion solution. This is a form of regularised solution where the regularisation parameter is given by 1/*M*. There are various ways of choosing *M*. A simple way, if one has an estimate of the 2-norm of *f*, say *E*, and an estimate of the 2-norm of the noise, *e*, is to choose *M* to be the largest integer, *k*, such that $\alpha_k^2 \geq (e/E)^2$ (Bertero and Boccacci, 1998). Other ways of choosing *M* are discussed, for example, in Hansen, 1998. Choice of this truncation point within the context of the gravity inverse problem is discussed in Paoletti et al. (2014) and Paoletti et al. (2016).

For practical problems the data are discretely sampled and in order to solve an inverse problem on a computer the object also has to be discretised, albeit finely. We then end up solving the discrete form of (1), namely

$$\mathbf{g} = \mathbf{K}\mathbf{f} , \tag{11}$$

where **K** is a matrix and **g** and **f** are vectors. The matrix **K** possesses a singular-value decomposition $\{\alpha_i, \mathbf{u}_i, \mathbf{v}_i\}_{i=1}^{N}$, where the α_i are the singular values, the $\mathbf{u}_i$ are the right-hand singular vectors and the $\mathbf{v}_i$ are the left-hand singular vectors (see Stewart, 1973 or Golub and Van Loan, 1993). The value, *N*, of the index *i* is the rank of **K**.

In an analogous way to the continuous problem, the singular-value decomposition may be used to solve the inverse problem specified by (11), and if the problem is ill-conditioned then a truncated singular-vector expansion may be employed, giving a solution to (11) of the form

$$\tilde{\mathbf{f}} = \sum_{k=1}^{M} \frac{b_k}{\alpha_k} \mathbf{u}_k , \tag{12}$$

where the coefficients b_k are given by

$$b_k = \mathbf{g} \cdot \mathbf{v}_k . \tag{13}$$

Now let us concentrate on the use of the singular-value decomposition in two-dimensional gradiometry, i.e. we will use it to solve (3) with z' fixed. We will assume that the horizontal coordinate is *x* and the vertical one is *z*, where positive *z* corresponds to the upwards direction. To convert these two coordinates into one we use a lexicographic mapping, and the previous one-dimensional theory is then applicable.

We will assume that the source of the anomaly lies in a rectangular box of known size underneath the horizontal line along which the data are recorded. The right-hand singular functions will then be

defined in this box, which we term the reconstruction box. For practical purposes it is desirable to have a reconstruction box of somewhat greater width than the horizontal region over which the data are acquired. This takes into account possible gravitational signals from objects that lie just outside the region within which the data are taken. In this paper, for the two-dimensional problem, we use a reconstruction box with a width of twice the horizontal extent of the data.

For our initial simulations we consider 100 data points acquired at *z*= 1.5m. The points are spaced by 0.1m from *x*= -4.9m to *x*= 5m. We note that the data do not have to be regularly sampled in order to use this method, but we do so here for simplicity. The size of the reconstruction box in terms of grid points is 200 in *x* by 20 in *z*. The grid point spacing is 0.05m in *x* and 0.5m in *z*. The bottom left grid point is at *x*= -9.95m, *z*= -10m and the top right point is at *x*= 10m, *z*= -0.5m. We treat the discrete problem as a close approximation to the continuous problem and hence we refer to the singular vectors as singular functions. Similarly, we use the notations in (10) and (12) somewhat interchangeably.

We show plots of the first three right-hand singular functions of the operator in (3) in figure 1 together with the first three left-hand singular functions. The singular functions are normalised such that, when they are viewed as vectors, the sum of the squared components is unity. Note that in these, and all later plots in the reconstruction box, interpolation has been use to convert from the point-sources in the solution to continuous functions.

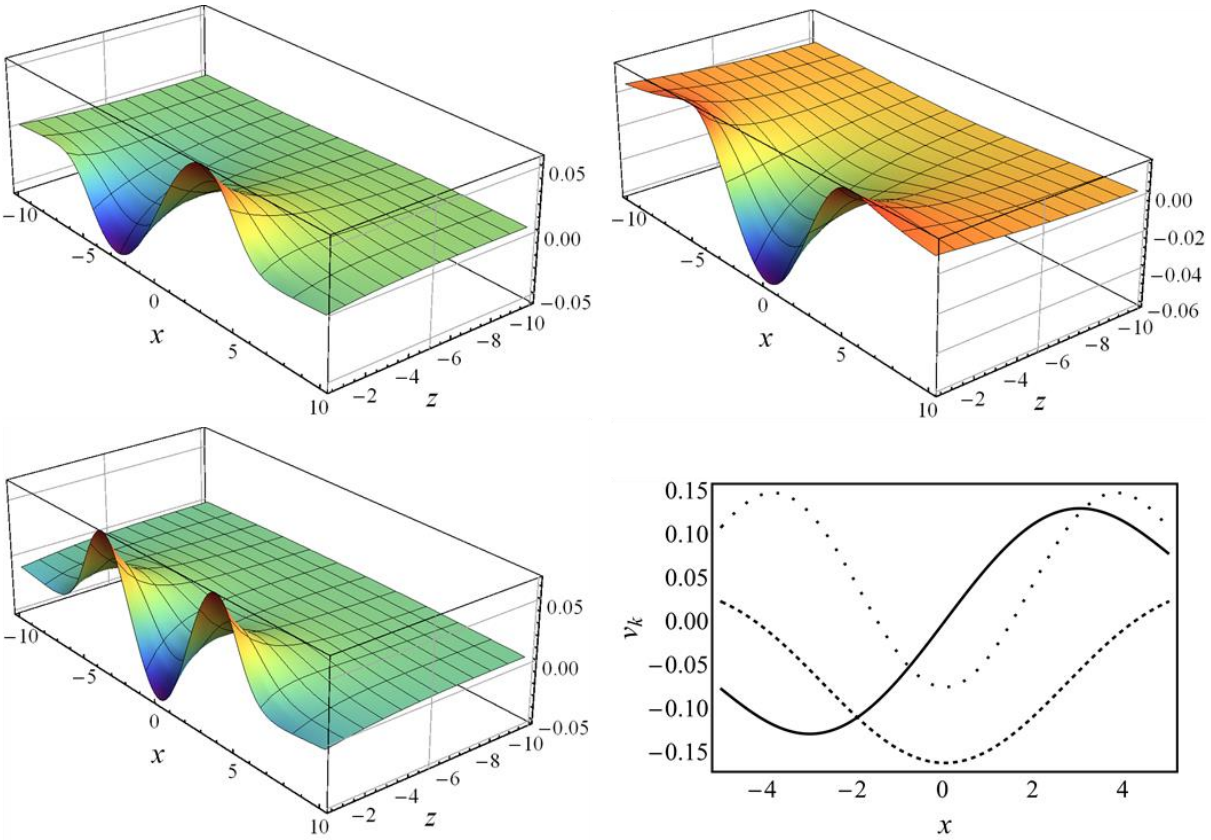

Figure 1. Top left - the first right-hand singular function, u_0*, top right – the second right-hand singular function,* u_1*, bottom left – the third right-hand singular function,* u_2*, bottom right – the first three left-hand singular functions; first left-*

hand singular function, v_0, full line, second left-hand singular function, v_1, dashed line, third left-hand singular function, v_2, dotted line. All coordinates are in m.

As the index of the singular values increases, both sets of corresponding singular functions become more oscillatory. The *n*th right-hand singular function has *n*+1 zero crossings at the surface of the reconstruction box. The only exceptions to this are the first two. We note also that the more oscillatory the right-hand singular functions are, the faster they decay with depth. Hence the more oscillatory ones, which correspond to the smaller singular values, tend to correspond to features nearer the surface.

It is worth at this point revisiting the questions of sampling density for the data and positioning of grid points in the reconstruction box. The fact that there is a dimension mismatch between the data and object spaces means that the inverse problem is not well-defined and that the structure of the right-hand singular functions depends strongly on the sampling strategy for the data and the positioning of the grid points in the object space.

Suppose we choose the data samples and the horizontal grid points to have the same spacing. Let there be n_d data samples, n_x horizontal grid points and n_z vertical grid points, where we assume that n_x does not change with depth. We find that, provided $n_d \leq n_x$, all the right-hand singular functions have a roughly exponential decay with depth. If, on the other hand, we have $n_d > n_x$ then, provided there are precisely n_d singular values (where, by definition, singular values must be strictly positive), mutual orthogonality of the right-hand singular functions means that they must oscillate in depth (provided $n_z > 1$). This idea is explored in Fedi et al., 2005, where the concept of the depth-resolution plot is introduced. Another alternative, which we do not explore here, is to let n_x decrease with depth, reflecting the fact that the expected resolution decreases with depth.

We can summarise by reiterating that the positioning of the grid points is a form of prior information about the object's likely structure. In this paper we follow the first of the above alternatives, leading to a roughly exponential decay of the right-hand singular functions with depth. This decay with depth provides an equivalent explanation as to why the generalised solution, given by (8) for one-dimensional problems, also decays rapidly with depth.

4. The use of prior information

Given that ill-posed inverse problems have a wide range of solutions one way of categorising these is via prior information. For potential fields this approach is followed in Cella and Fedi, 2012. In the previous section we saw that the choice of the size and shape of the reconstruction box is a form of prior information. Once these are fixed one still has flexibility in how the grid points are chosen inside this box. This is classed in Cella and Fedi as prior information on source-volume discretisation.

Other forms of prior information can be knowledge of the density of the source of the anomaly, or knowledge that it resembles the solution to the inverse problem with minimum support (Portniaguine and Zhdanov, 1999).

Imaging methods, mentioned in the introduction, which depend on the structural index, such as the depth from extreme points method, can be thought of as using prior information that the source has a simple structure, for which the structural index is well-defined.

Weighting methods, such as that introduced by Li and Oldenburg (1996), can be thought of as using the prior information that the source does not lie at the surface.

In this paper we use a different kind of prior information, namely that the object lies at a single depth but this depth is unknown. It is important to point out that this prior information does not give us a unique solution; rather, we give a range of solutions at different depths and further prior information must be used to restrict this range further.

5. The profiled singular-function expansion

We introduce the profiled singular-function expansion by looking first at a general one-dimensional linear inverse problem with continuous data, specified by the integral equation (1). The basic mathematics may be found in Bertero et al. (1985).

Suppose we have a positive function *P(s)* which we term the profile. Instead of assuming that the solution *f* lies in $L^2(a,b)$ we now assume that it satisfies the condition

$$\int_a^b \frac{f^2(s)}{P^2(s)} ds < \infty. \tag{14}$$

We choose *P(s)* to reflect the prior information we have about where the solution is small. So, for example, if we believe the solution to be negligible at the ends of the interval [*a, b*] we can choose *P(s)* to be very small at *a* and *b*.

Now suppose that *f* satisfies (14) and put

$$f(s) = P(s)\psi(s). \tag{15}$$

We then have $\psi(s) \in L^2(a,b)$ and substituting (15) in (1) we find that $\psi(s)$ satisfies

$$g(y) = \int_a^b K(y,s)P(s)\psi(s)ds \equiv (L\psi)(y), \quad c \le y \le d. \tag{16}$$

We denote the singular system of the operator *L*, viewed as an operator from $L^2(a,b)$ to $L^2(c,d)$, by $\{\alpha_k; \psi_k, v_k\}_{k=0}^{\infty}$. Note that, for convenience, we have used the same notation for the singular values and the left-hand singular functions as in the un-profiled case. We may then solve the inverse problem specified by (16):

$$\tilde{\psi}(s) = \sum_{k=0}^{\infty} \frac{b_k}{\alpha_k}\psi_k(s), \tag{17}$$

where

$$b_k = \langle g, v_k \rangle_G . \tag{18}$$

This is the generalised solution to (16). In the presence of noise (17) needs to be truncated:

$$\tilde{\psi}(s) = \sum_{k=0}^{M} \frac{b_k}{\alpha_k}\psi_k(s) , \tag{19}$$

where the truncation point *M* depends on the noise level. The solution to (1) then takes the form

$$\tilde{f}(s) = \sum_{k=0}^{M} \frac{b_k}{\alpha_k} P(s)\psi_k(s). \tag{20}$$

Thus we can see that the overall shape of the solution involves a factor of *P(s)*.

Turning now to the case of discrete data, (1) now becomes

$$g(y_n) = \int_a^b K(y_n, s) f(s) ds, \quad 1 \le n \le N . \tag{21}$$

If we demand, as before, that *f* should satisfy (14) then we can again write *f* in the form (15) and (21) becomes

$$g(y_n) = \int_a^b K(y_n, s) P(s)\psi(s) ds \equiv (L_N \psi)(y_n), \quad 1 \le n \le N . \tag{22}$$

We now perform the singular-value decomposition of L_N. We denote this by $\{\alpha_{N,k}; \psi_{N,k}, \mathbf{v}_{N,k}\}_{k=0}^{N-1}$. Let us define a data vector **g** by $g_n = g(y_n), 1 \le n \le N$. The generalised solution to (22) is then given by

$$\tilde{\psi}(s) = \sum_{k=0}^{N-1} \frac{b_k}{\alpha_{N,k}} \psi_{N,k}(s), \tag{23}$$

where

$$b_k = \mathbf{g} \cdot \mathbf{v}_{N,k} . \tag{24}$$

As with the continuous-data problem the determination of the generalised solution may be ill-conditioned and the expansion in (23) may need to be truncated at a point *M* determined by the noise level. This then gives, as a solution to (21),

$$\tilde{f}(s) = \sum_{k=0}^{M} \frac{b_k}{\alpha_{N,k}} P(s)\psi_{N,k}(s). \tag{25}$$

Now let us apply this to the two-dimensional gradiometry problem. Once again, the two variables *x* and *z* can be mapped into the one-dimensional variable *s* and the preceding mathematics can be used. To achieve a solution which is not concentrated near the top of the reconstruction box we introduce a depth profile in *z* which can have a peak at any chosen value of *z*. We choose a Gaussian profile centred on the depth at which we expect our solution to lie. By varying this depth we can reconstruct a range of solutions at different depths. To some extent, the use of a Gaussian profile, rather than some other profile, is also making a prior assumption about the nature of the solution, i.e. that it has a maximum density somewhere near the peak of the Gaussian and falls away gradually from that peak.

Note that if our reconstruction box was, say, of the same horizontal extent as the data this would typically lead to a sharp cut-off of the solution at the sides of the reconstruction box. This could be controlled by also introducing a profile in *x*, which would be an alternative to the approach we have adopted of using a reconstruction box which is wider than the data region.

We show in figure 2 two profiles, one corresponding to the depth in the middle of the reconstruction box and one corresponding to the depth at the bottom.

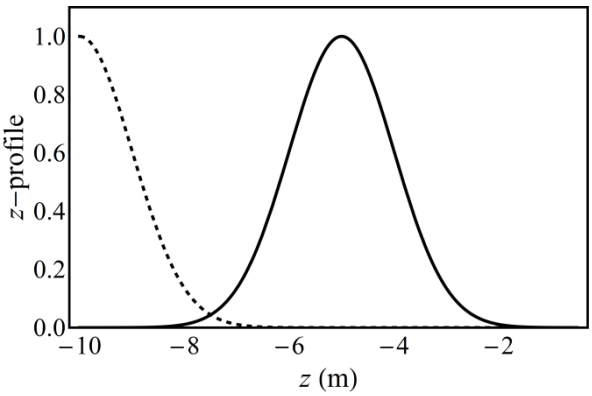

Figure 2. Two depth-profile functions used, dotted line: peak at z=-10m; solid line: peak at z=-5m.

Both profiles have a 1/*e* half-width of $\sqrt{2}$ m. In figure 3 we show the first three right-hand singular functions for the middle profile together with the corresponding left-hand singular functions. The first three right-hand singular functions for the deepest profile are shown in figure 4 together with the corresponding left-hand singular functions. Table 1 lists the first 10 singular values for all three situations: no profiling, profile centred at *z*=-5m, and profile centred at *z*=-10m.

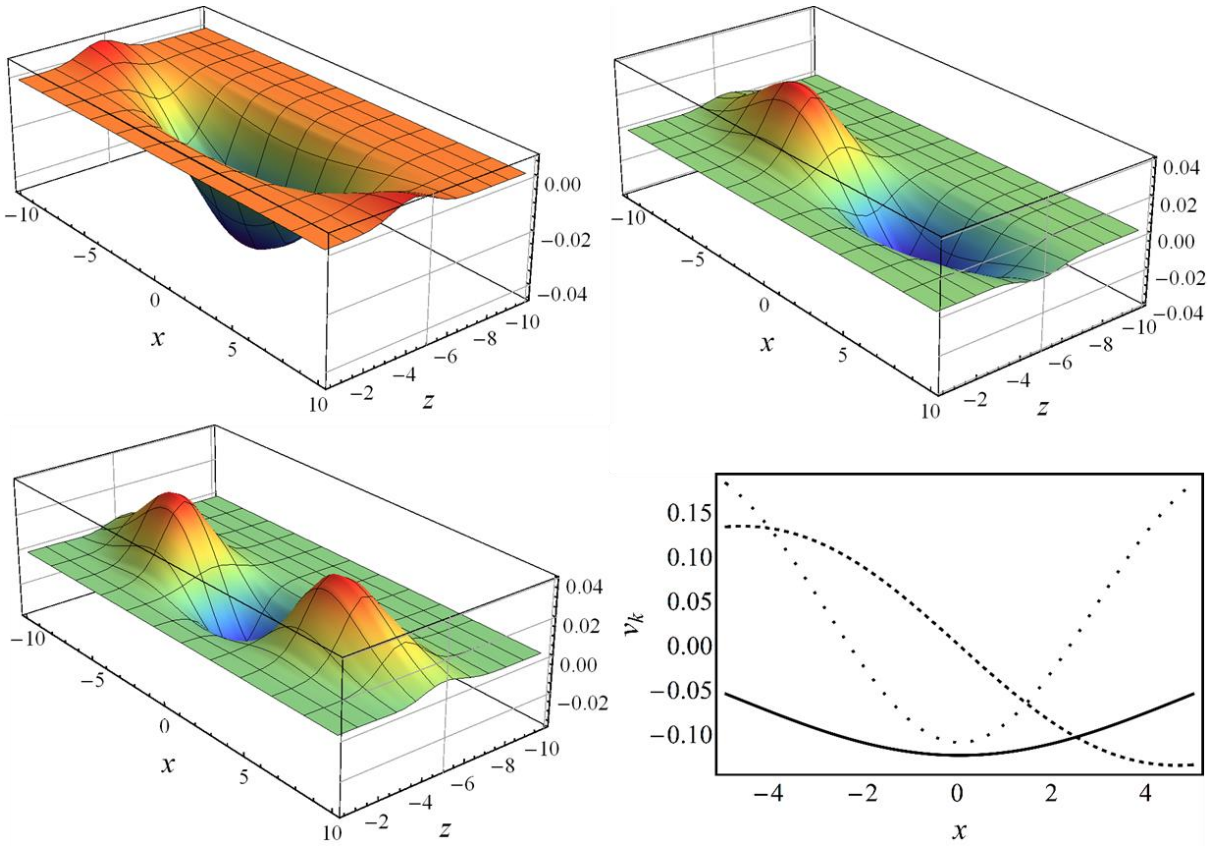

Figure 3. Top left - the first right-hand singular function, ψ_0, for the middle depth profile. Top right – the second right-hand singular function, ψ_1. Bottom left – the third right-hand singular function, ψ_2. Bottom right – the first three left-hand singular functions; solid line: first left-hand singular function, v_0; dashed line: second left-hand singular function, v_1; dotted line: third left-hand singular function, v_2. All coordinates are in m.

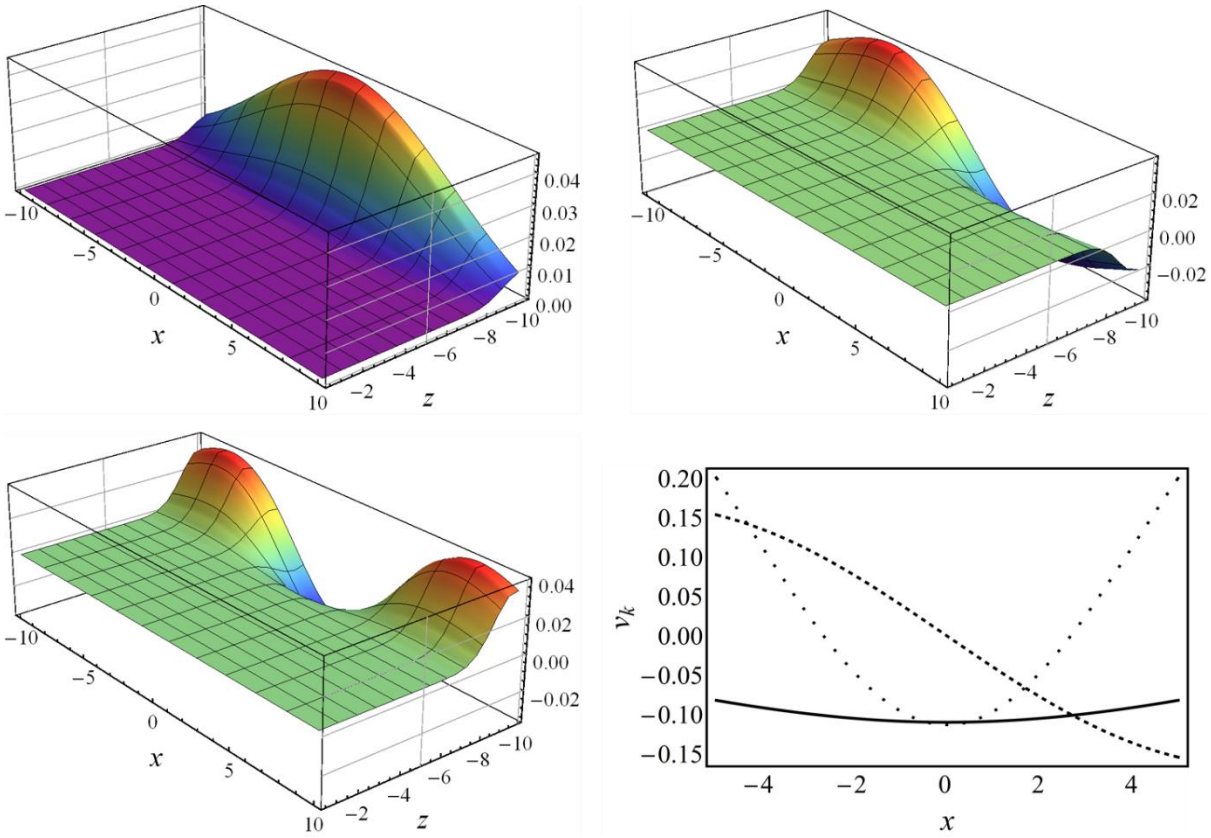

Figure 4. Top left - the first right-hand singular function, ψ_0, for the deepest profile. Top right – the second right-hand singular function, ψ_1. Bottom left – the third right-hand singular function, ψ_2. Bottom right – the first three left-hand singular functions; solid line: first left-hand singular function, v_0; dashed line: second left-hand singular function, v_1; dotted line: third left-hand singular function, v_2. All coordinates are in m.

	0	1	2	3	4	5	6	7	8	9
Top	24.9	23.9	18.5	14.4	9.823	6.79	4.46	2.96	1.90	1.23
Middle	7.08	5.15	2.15	0.904	0.330	0.126	0.0457	0.0173	0.00649	0.00253
Bottom	2.84	1.23	0.282	0.0625	0.0119	0.00231	0.000421	7.89E-05	1.45E-05	2.77E-06

Table 1.The first ten singular values for the different profile functions (top corresponding to no profiling).

Clearly, the depth profile is, as intended, shifting the right-hand singular functions, and thus the solution, away from the surface. From table 1 we observe that the rate of decay of the singular values increases as the profile is moved to greater depth, reflecting that fact that less information arrives at the surface from greater depths. Note that, for convenience, we set the gravitational constant, γ, to unity in the modelling and this is reflected in the values in the table.

6. Simulated reconstructions

To show the operation of the depth-profiling method, we consider a simple object consisting of two squares of density contrast +1000 kg/m^3, both centred at depth *z*=-5m and separated by 5m in *x*. We used the following formula for the vertical gravity gradient from a rectangular prism of infinite length:

$$g(x',z') = -2\gamma\rho\left\{\tan^{-1}\left(\frac{a-2(x-x')}{c-2(z-z')}\right)+\tan^{-1}\left(\frac{a-2(x-x')}{c+2(z-z')}\right)+\tan^{-1}\left(\frac{a+2(x-x')}{c-2(z-z')}\right)+\tan^{-1}\left(\frac{a+2(x-x')}{c+2(z-z')}\right)\right\} \quad (26)$$

Here ρ is the density contrast and the rectangle is centred at *x*, *z*, with width *a* and height *c*. Equation 26 was derived from the result for a 3D cuboid (given in Commer, 2011) by taking the limit as the length in the *y*-direction goes to infinity.

We assume that the depth of the object is known, so that a matching profile may be chosen (i.e. the solid line in figure 2). The background density is taken to be zero, which is equivalent to assuming that the background gravity gradient signal has been subtracted off. Given that the density contrast of the unit squares is +1000 kg/m^3 we have that the maximum gravity gradient signal, at the height of the detector z'=1.5m, from a single square is 3.16Eo (from (26)).

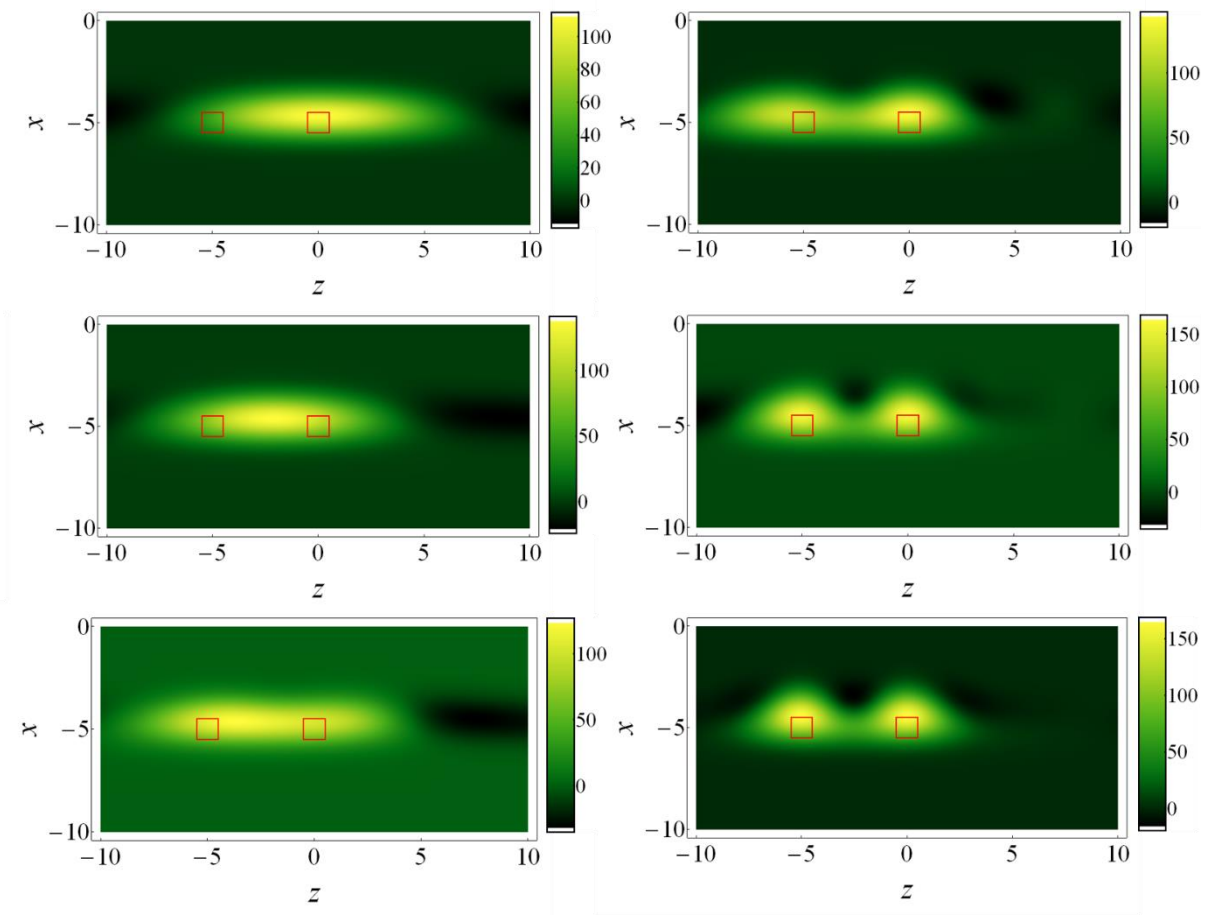

Figure 5. Solutions for two squares of unit dimension with centres at x=-5m and 0, separated by 5m. From top to bottom, first column, using 1, 2 and 4 singular functions; second column, using 5, 10 and 49 (all significant) singular functions. The units are kg/m³.

As the number of singular functions is increased, the two squares become distinguishable as two separate objects. In this example, the squares are almost indistinguishable from point sources; thus the two separate 'blobs' can be taken to represent 'point-spread functions' and we can say that, when enough singular functions are used, the resolution is sufficient to resolve points separated by 5m. This agrees with the conventional wisdom that two identical anomalies at the same depth can be resolved if their horizontal separation is approximately equal to, or greater than the depth (Hinze et al., 2013, Chapter 7, section 3.1). Note, however, that the extent of the point-spread function in the depth axis is simply that imposed by the width of the profile function.

In the top plot of figure 6 we show approximations to the true data corresponding to the object used for figure 5, using different numbers of left-hand singular functions. It can be seen that even with only 4 singular functions agreement with the data is quite good. In order to quantify this, we define a relative fitting error ε by

$$\varepsilon = \frac{\left\| \mathbf{g} - \mathbf{K}\tilde{\mathbf{f}} \right\|_2}{\left\| \mathbf{g} \right\|_2}. \tag{27}$$

This fitting error is plotted in the bottom plot of figure 6 as a function of the number of singular functions used. Note the use of the logarithmic scale, which indicates that the fitting error (27) reduces very rapidly as the number of singular functions is increased. In practice, this means that the

contributions of higher-index singular functions to the reconstructed object will be rapidly obscured by any noise on the data. This suggests that, in a practical application, only the first few singular functions could be used: higher-index left-hand singular functions would just fit the noise in the data and would lead to obscuration of the real object in the reconstruction.

Note that although there are 100 data points only 49 singular values and vectors are returned by the SVD routine used. The singular values decay rapidly and that with index 49 is of the order of 10^{-13}. After that machine precision issues preclude the calculation of further singular values and vectors.

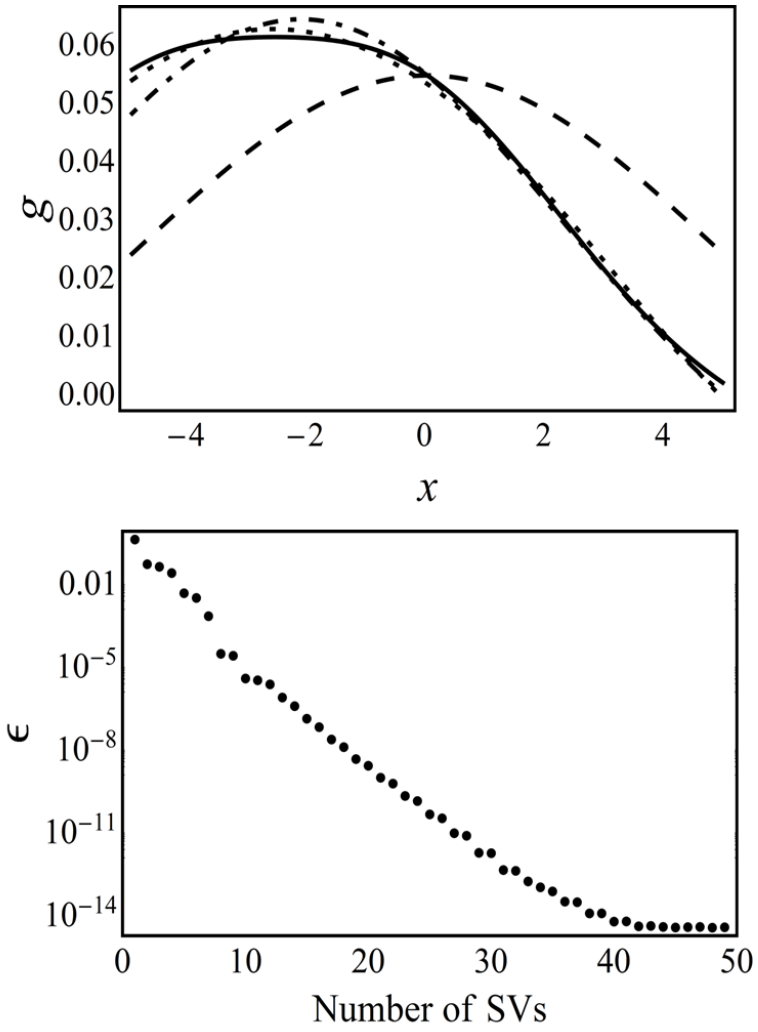

Figure 6. Top plot: solid line is the data; dashed line is the approximation using just the 1st left-hand singular function; dash-dotted line uses the first 2 left-hand singular functions; dotted line uses the first 4 left-hand singular functions. Bottom plot: the relative fitting error versus the number of singular functions used.

With reference to figure 5, it is interesting to note that the resolution of the reconstructed object does not noticeably improve as the number of right-hand singular functions is increased beyond 7:

the sizes of the 'blobs' representing the original squares do not reduce further. This behaviour is different to what is usually seen in non-profiled SVD, where the addition of higher-order right-hand singular functions improves resolution. The reason for this discrepancy can be seen in the results shown in figures 7 and 8. Here we show, on the left-hand side, various right-hand singular functions. On the right-hand side we show these singular functions multiplied by the profile function, as they will appear in the solution in (25). The key thing to note here is that, as the index increases, the right-hand singular functions have a tendency to move towards the top of the reconstruction region. Thus, when multiplied by the depth profile, the detail in the centre of the right-hand singular functions becomes progressively washed out. Hence, one might expect that, beyond a certain point, adding more singular functions will not yield a corresponding increase in resolution in (25) and indeed this is what we find. The additional degrees of freedom associated with the higher-index singular functions are not appearing at the depth at which the object is being reconstructed and therefore are not leading to greater resolution.

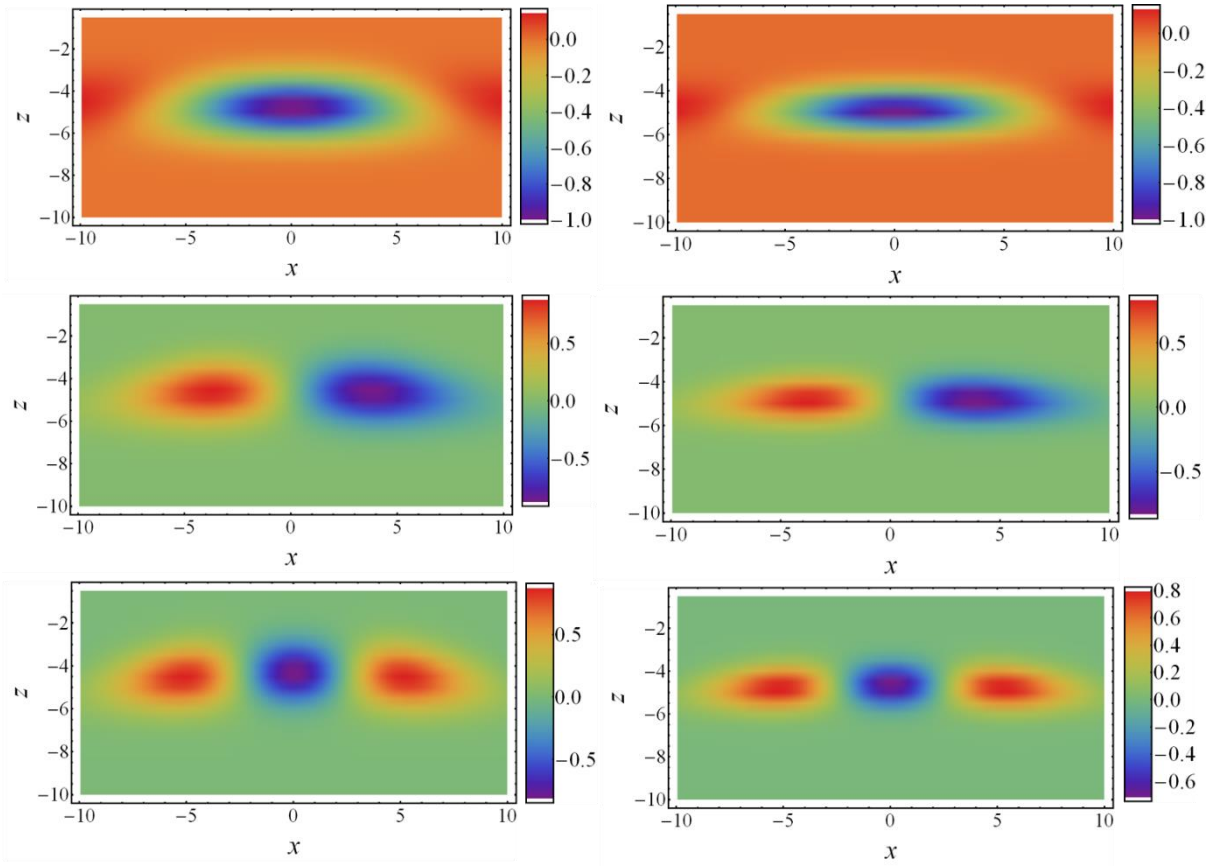

Figure 7. The first three right-hand singular functions: Left column, before the profile is applied; Right column, after the profile is applied. The colour scales are normalised by the maximum of the absolute value of the first singular function.

One might be tempted to try to overcome this limitation by using a rectangular profile function, thus forcing all the right-hand singular functions to lie at the depth of interest. However, the net effect of doing this would be the same as shifting the top of the reconstruction box to a lower level and the right-hand singular functions would again be concentrated at the top of the new reconstruction box and have a roughly exponential fall-off, as in the un-profiled case. Of course, this could still give a valid solution to the inverse problem, so, again, it would come down to prior information as to whether such a solution is considered more or less likely than the solution produced with the Gaussian profile. In the absence of prior information that tells one there is actually a sharp boundary

in the object density at a given depth, it seems undesirable to impose one so drastically in the solution. When a rectangular-profiled solution is calculated, we find that the corresponding point-spread function can be narrower in the *x*-direction than in the results given in figure 5 for the Gaussian profile. This implies a potentially better resolution; however, this may have no practical relevance because it requires the use of higher-index singular functions which have very small associated singular values, implying an unrealistically low level of noise on the data.

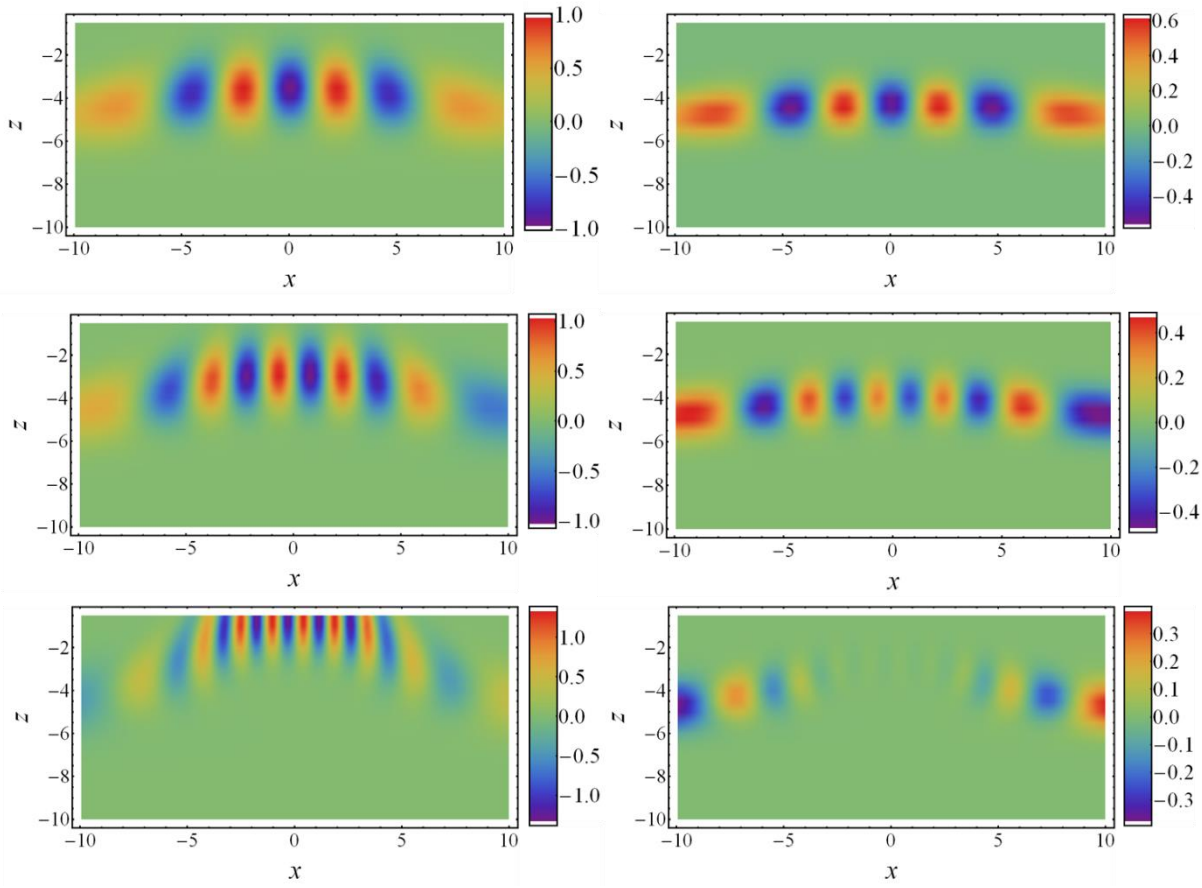

Figure 8 – the right-hand singular functions with index 7, 10 and 18: Left column, before profile is applied; Right column, after profile is applied. The colour scales are normalised by the maximum of the absolute value of the first singular function.

7. Varying the profile depth

It was shown in the previous section that the depth-profiling method can be used to produce a reconstructed object, the depth of which is known in advance. Now we consider the case of an isolated anomaly from an object at unknown depth and we ask the question whether or not the profiling method allows one to extract depth information. Figure 9 shows reconstructions of a single square at depth z=-5m using depth-profiles of the same width as in the previous section but with different peak positions, z_p (the plots employ the same colour scaling as in figure 5).

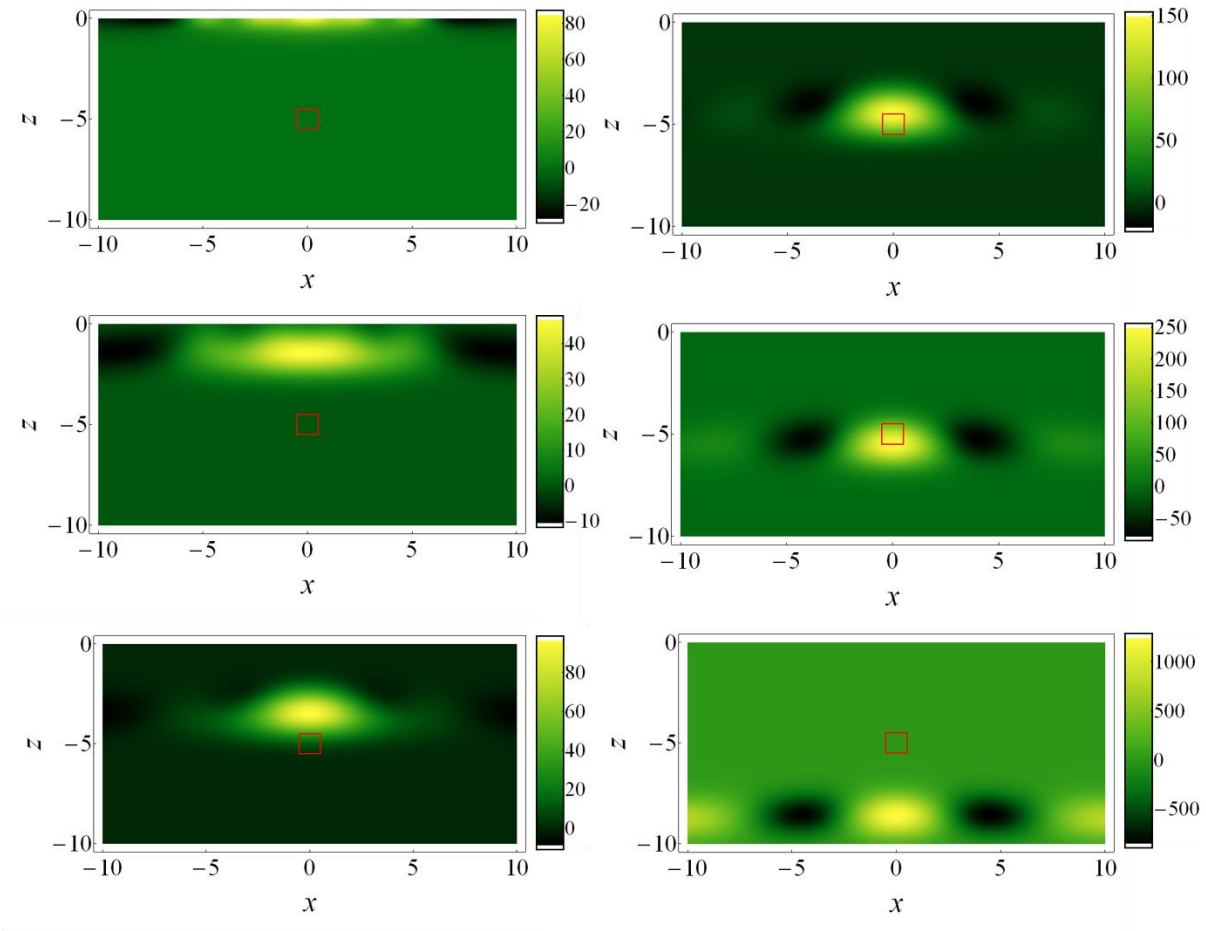

Figure 9 – Reconstruction of single square at z=-5m. Depth profiles for the left-hand column are centred at 0m, -2m and -4m. Depth profiles for the right-hand column are centred at -5m, -6m and -9m. The units are kg/m³.

Here, the singular-function expansion was truncated to account for the effect of the additive noise that would be present in a real measurement, although no actual noise was included in the simulation. The procedure was as follows: for each profile depth, z_p, the number of singular functions used in the expansion was increased until the error metric of (27) dropped below 0.01. This means that the terms in the left-hand singular function expansion that are neglected have a norm that is less than 0.01 of the norm of the data, and would, therefore, be lost in the noise on the data, if there were noise at this level. In other words, approximately speaking, the solutions in figure 9 are those that would be obtained if the signal-to-noise ratio was of order 100:1. This procedure resulted in 9 singular functions being used when the profile peak was at the top of the reconstruction box, dropping to 5 at the bottom of the box. Note that, owing to the even symmetry of the anomaly, only odd-numbered singular functions contribute to the solution, so the number reduces from 9 to 7 then 5.

It can be seen in figure 9 that the most compact (or focused) reconstruction occurs for those profiles with peaks near the true depth of object. Near the surface the solution has a greater spread in the *x* direction. Below the depth of the object the solution has a narrower central lobe but significant multiple side-lobes. Overall we consider the latter to be less compact owing to the large sidelobes. It should be emphasised that all of these may be good solutions if they fit the original data well; however, these results suggest that if one is expecting a simple object (i.e. we have prior knowledge) some depth information may be inferred. We note that a small number of objects at the same depth (as in figure 5) would also show this focussing behaviour, because the inversion is linear.

Prior knowledge about the range of densities can also be used to rule out solutions at greater depths: a point noted in Roy, 1962, for the case of infinite data. The maximum and minimum values of the density contrast in the solution are given in Table 2 for each of the values of the depth-profile peak.

z_p(m)	0	-1	-2	-3	-4	-5	-6	-7	-8	-9
Max	-85	47	47	66	96	149	249	423	724	1024
Min	-28	-15	-11	-11	-9	-20	-79	-200	-430	-860

Table 2. Maximum and minimum density contrast values for the solutions with different profile depths in kg/m³.

For comparison, the object density contrast was 1000 kg/m^3. Note that the reconstructed maximum density contrast when the profile is at the correct depth is 149 kg/m^3. The reason this is substantially smaller than the object density is because the solution occupies a larger area than the actual object and therefore represents a blurred version of it. For ill-posed problems it is perfectly natural that a linear inversion method should deliver such a blurred solution. It can be seen that the range of the contrast values increases rapidly for depths below the actual object. Large negative values of density, appearing in the side-lobes, could be used to rule out deeper solutions on the basis that they are unphysical.

8. 3D simulation results

As mentioned previously, the profiled SVD can easily be extended to 3D inversion. Consider an underground void as shown in figure 10. The density of the surrounding medium is taken to be 2000 kg/m^3 and the surface lies at z = 0. The void is centred at z = -5m and has a maximum thickness in depth of 3m. The data are recorded 0.5m above the surface. We carry out an SVD of the appropriate gradiometry kernel. We choose a reconstruction box with horizontal dimensions 3/2 times the sides of the data region. We do not show figures of the singular functions. However, as with the 2D problem the right- and left-hand singular functions become more oscillatory as their index increases. Furthermore, in the unprofiled case the left-hand singular functions decay roughly exponentially with depth, the rate of decay increasing with their index.

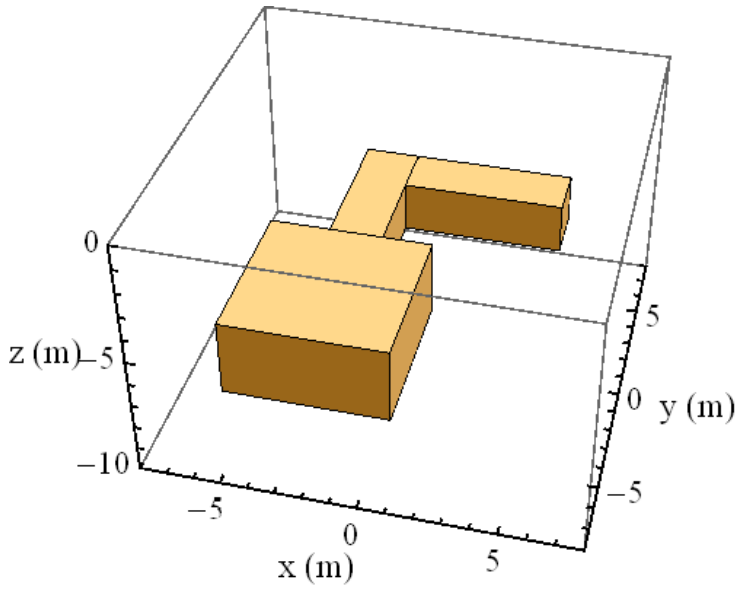

Figure 10. The simulated underground void.

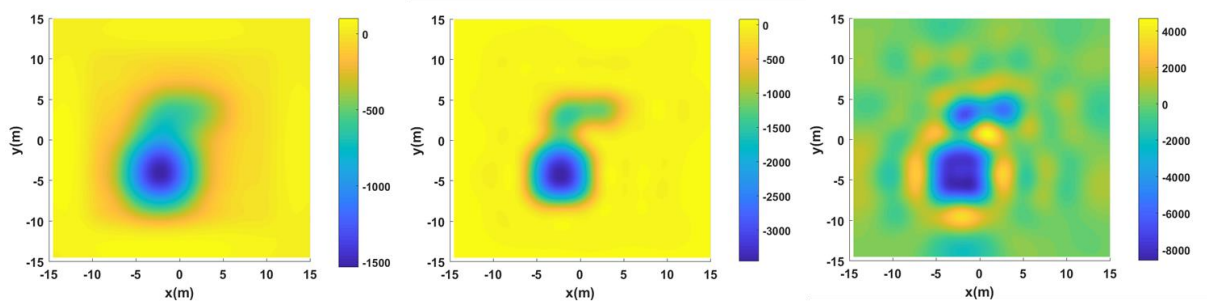

Figure 11. Reconstruction at (a)3m depth, (b) 5m depth and (c) 7m depth. 100 singular functions were used in each case.

We consider a range of Gaussian profiles with a 1/e half-width of $\sqrt{2}$ m. 2D horizontal cross-sections are given in figure 11 for three different profile depth positions and a fixed number of singular functions used in the reconstruction. In each case, the depth of the 2D cross-section corresponds to the centre of the profile function. The colour scale has units of kg/m^3. In 11(a) the peak of the profile function is 2m above the centre of the structure. It can be seen that this reconstruction is smoother than the one in 11(b), for which the profile function is peaked at the centre of the structure. In 11(c) the peak of the profile function is 2m below the centre of the structure. This results in a reconstruction with significant sidelobes, as in the 2D case discussed in section 7. In addition the range of the density values is physically unrealistic, which rules this out as a possible solution. So using the a priori assumptions that the solution should have physically realistic density values and be tightly focussed results in a solution which is at the correct depth and which shows most clearly the shape of the structure (at least, the shape in horizontal cross-section: the vertical shape tends to follow that of the depth profile).

Note that, although our structure has a significant thickness in depth, it is still sufficiently thin to be treated as quasi-two-dimensional. Too much depth variation would cause problems for this technique; for example, it is necessary for there to be a region of uniform density between the top of the structure and the measurement plane: any additional density variations near the surface would 'interfere' with the reconstruction.

9. Experimental data

To confirm that our approach has some validity on real data we used some data from a microgravity survey carried out over the Broadway Tower nuclear bunker in Worcestershire, England. This is essentially a rectangular box of 2.25m height, 2.27m width and 5.46m length. The centre of the bunker is 3.08m below ground level. The underlying bedrock is the Inferior Oolite. Data for a transect across the centre of the bunker were recorded using a Scintrex CG-5 gravimeter. Three 30-second readings were collected for each point, and the results were averaged to produce the final gravity value. The location and heights of the measurements, along with the ground surface, were recorded using a surveying total station and laser-scanning equipment. The readings were corrected by the instrument's internal algorithms to account for temperature, tilt and tidal effects, and using the collected location and height data to account for the latitude, free-air correction and the gravity effects of the surrounding terrain. A regional trend was also removed from the data using a linear fit. The inverse problem was treated as a 2-dimensional one with roughly 10% noise, though some of the data were considerably noisier.

We show, in figure 12, reconstructions for different profile depths, normalised so that the peak corresponding to the bunker has the value -1. The three Gaussian profiles were centred at depths of 0.9m, 3.0m and 5.4m. Each profile had a 1/*e* half-width of 1.15m. We used 9 singular functions for

the top reconstruction and 6 singular functions for the lower ones. We see that the peak corresponding to the bunker narrows as we go to greater depths, but the sidelobes grow, until, for the deepest profile, one of the sidelobes is almost as large in magnitude as the main peak. Compared to our gradiometry simulations we also see that there are significant sidelobes in the middle depth reconstruction. These could be due to the fact that the actual object is not confined to a narrow layer. These may be reduced by using fewer singular functions, at the expense of poorer horizontal resolution.

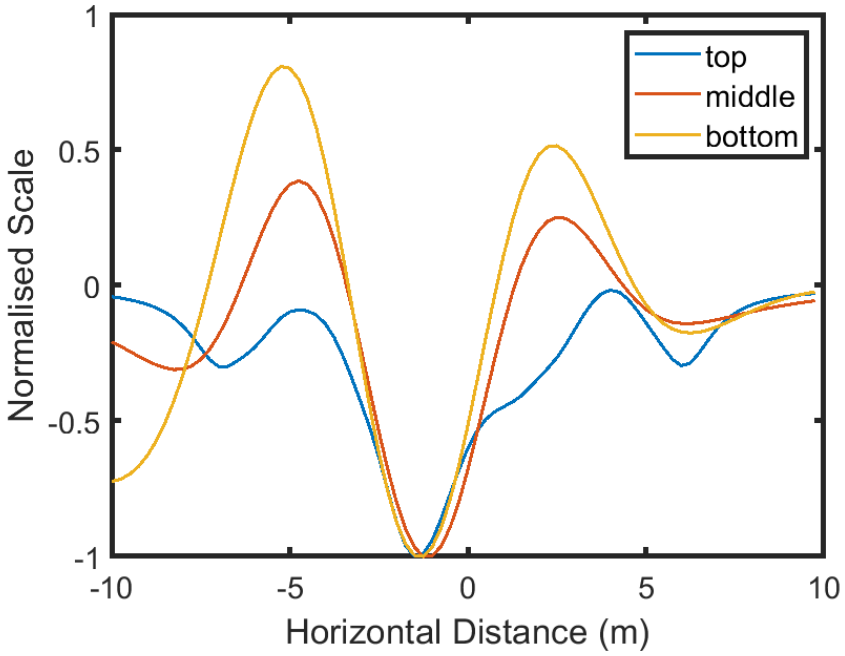

Figure 12. Reconstructions for different profile depths, normalised so that the central peak has the value -1.

We show in figure 13 the data and the reconstructed data for the three depths.

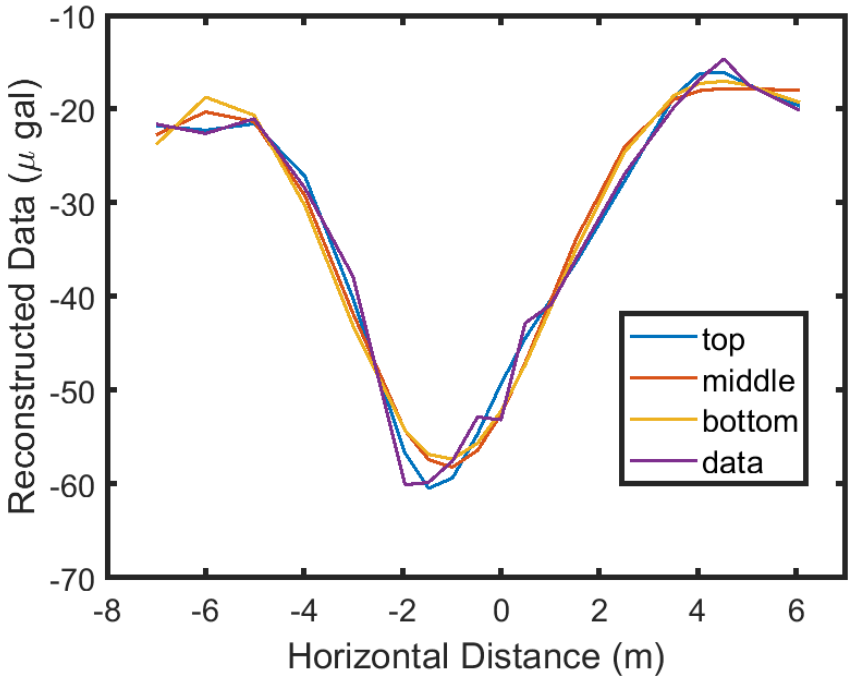

Figure 13. Fits to the data for the three different reconstructions shown in figure 12.

We see that all three reconstructions fit the data to within a 10% noise level. We show in figure 14 the reconstructions in the same format as fig. 9. As expected, the reconstructed density contrast rises dramatically for the profile below the correct depth.

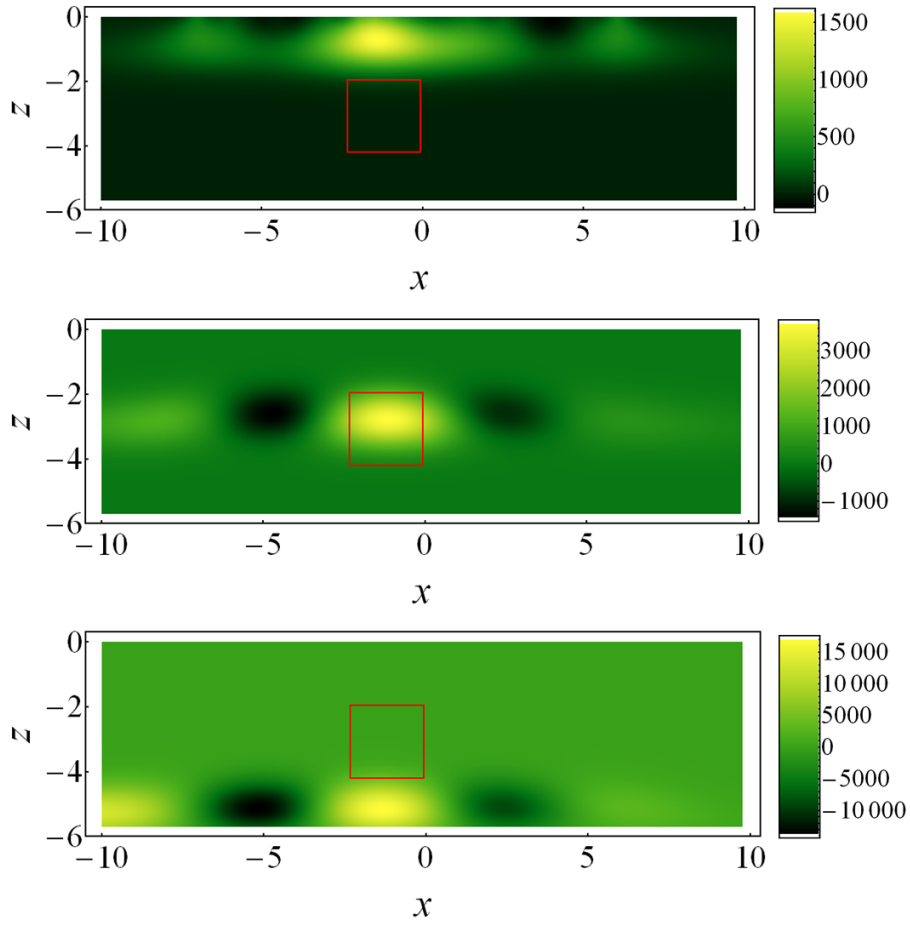

Figure 14. Reconstruction of bunker. Profiles centred at 0.9m, 3m and 5.4. The axes are in m. The units are kg/m³.

10. Discussion and conclusions

In this paper we have proposed a method of inverting gravity data, based on profiled singular-function expansions, which addresses the tendency of certain reconstruction algorithms to produce solutions which are concentrated near the surface of the reconstruction region. We have shown that this method has the potential to deal with ambiguities in gravity inversion problems via the inclusion of prior knowledge. In 2D simulations, we have used it to produce a solution at the correct depth when the depth is known a priori. We have also shown that, by producing and comparing solutions at different depths, the method can be used to extract some depth information when there is no prior knowledge of depth (except that the object lies within the reconstruction box), but the object is known to have a simple, compact structure.

In the absence of a profile the standard SVD solution still fits the data, but always peaks near the top surface of the reconstruction box and decays roughly exponentially with depth. This behaviour is always encountered with direct-inversion methods which seek to find the generalised solution. The use of a profile ensures that the solution looks more plausible in that it is smooth (except when the profile peak is too deep), as one might expect for a linear inverse problem where the resolution is

limited by the noise level. We find that, for a simple object, the solution “looks best”, i.e. there are minimal side-lobes, when the profile matches the object’s depth. One could also say that the solution is most focused when the object and profile depths agree. Furthermore, if one knows that the density contrast has a fixed sign, then this prior information can be used to rule out the solutions with pronounced negative side-lobes. Solutions at depths below the true object may also be ruled out by prior knowledge of the range of densities.

It is now worth discussing the depth ambiguity in a slightly different way. Depth ambiguity in gravity is often demonstrated by considering infinitesimally thick layers at different depths (Skeels, 1947, Roy, 1962). If these layers lie above the object giving rise to the anomaly then an equivalent density distribution, which gives rise to the same data, may be found on each. In Roy, 1962, this is shown by use of Green’s equivalent layer theorem. Note that this involves layers and data of infinite horizontal extent. Furthermore, if an unlimited range of positive and negative densities are allowed, the same data can be produced by an infinitesimally thick layer *below* the actual object (Roy, 1962).

In the work reported here we have a similar situation; however, the equivalent objects are not confined to infinitesimally thick layers but rather have a shape in z which is governed by the profile shape. The truncation of the profiled singular-function expansion means that our equivalent objects are only equivalent to within the noise level on the data, which determines the truncation point. We also point out that we are dealing with data recorded over a finite region, contrasting with the depth ambiguity in Roy, 1962, where the data is of infinite extent. The final plot in figure 9 is an example of a case where the equivalent object lies below the actual object, which corresponds to Roy’s case of an unphysical density contrast which is allowed to oscillate between positive and negative values.

We note that the scenarios we have considered are rather simplified. In particular, we have assumed that the underground density is constant everywhere except for an isolated object concentrated in a narrow layer at a particular depth. In the real world, this will not generally be the case: the objects of interest may be at different depths and there may be other density variations that are not of interest but are big enough to obscure the objects of interest (i.e. ‘clutter’). If objects are sufficiently separated in the horizontal direction, separate reconstruction boxes may be used with independent depth profiles. The most difficult situation is when objects occupy the same horizontal position, but are at different depths. In this case, the gravitational signals will overlap and may be difficult to disentangle. Similarly, near-surface clutter may obscure deeper objects. High spatial frequencies in the data, arising from near-surface clutter, may be removed by spatial filtering or, equivalently, truncation of the singular-function expansion; however, the remaining lower-spatial frequencies may still obscure deeper objects of interest. Another difficult situation is when a single object is significantly extended in depth.

However, in spite of these difficulties, we conclude that the profiled SVD approach shows promise as a technique for interpreting isolated gravity anomalies lying at a particular depth and for resolving depth ambiguity in gravity inversion.

Acknowledgements

The authors would like to thank Gareth Brown for useful discussions. We would also like to thank the staff at Broadway Tower Country Park for their help while the survey was being undertaken. This work was funded by DSTL under the Gravity Imager project, contract number DSTLX-1000095040, and EPSRC contract number EP/M508378/1.

References

[1] V. C. F. Barbosa, J. B. C. Silva, and W. E. Medeiros, "Practical applications of uniqueness theorems in gravimetry: Part II - Pragmatic incorporation of concrete geologic information," *Geophysics,* vol. 67, no. 3, pp. 795–800, May 2002.

[2] M. Bertero and P. Boccacci, *Introduction to inverse problems in imaging*. Bristol and Philadelphia: Institute of Physics Publishing, 1998.

[3] M. Bertero, P. Brianzi and E. R. Pike, "On the recovery and resolution of exponential relaxation rates from experimental data: Laplace transform inversions in weighted spaces," *Inverse Problems,* vol. 1, no. 1, pp. 1-15, Feb. 1985.

[4] D. Boddice, N. Metje and G. Tuckwell, "Capability assessment and challenges for quantum technology gravity sensors for near surface terrestrial geophysical surveying", *J. Appl. Geophys.* Vol. 146, pp. 149-159, 2017.

[5] O. Boulanger and M. Chouteau, "Constraints in 3D gravity inversion," *Geophys. Prospecting,* vol. 49, no. 2, pp. 265-280, March 2001.

[6] G. Brown, K.D. Ridley, A.D. Rodgers and G.D. de Villiers, "Bayesian signal processing techniques for the detection of highly localised gravity anomalies using quantum interferometry technology," SPIE conference on Security and Defence, Edinburgh, 2016.

[6a] Cella, F., Fedi, M., 2012. Inversion of potential field data using the structural index as weighting function rate decay. Geophys. Prospect. 60, 313-336.

[7] M. Commer, "Three-dimensional gravity modelling and focusing inversion using rectangular meshes," *Geophys. Prospecting,* vol. 59, no. 2, pp. 966–979, Sept. 2011.

[8] J. Cribb, "Application of the generalized inverse to the inversion of static potential data," *Geophysics,* vol. 41, no. 6, pp. 1365-1369, Dec. 1976.

[9] M. Fedi, "DEXP: A fast method to determine the depth and the structural index of potential field source", *Geophysics*, vol. 72, I1-I11, 2007.

[10] M. Fedi, P.C. Hansen and V. Paoletti, "Analysis of depth resolution in potential-field inversion," *Geophysics,* vol**.** 70, no. 6, pp. A1-A11, Nov. 2005.

[11] M. Fedi and M. Pilkington, "Understanding imaging methods for potential field data," *Geophysics*, vol. 77, no. 1, pp. G13-G24, Jan. 2012.

[12] M. Fedi and A. Rapolla, "3-D inversion of gravity and magnetic data with depth resolution," *Geophysics*, vol. 64, no. 2, pp. 452-460, March 1999.

[13] G.H. Golub and C.F. Van Loan, *Matrix computations, 2nd edition.* Baltimore: The Johns Hopkins University Press, 1993.

[14] P.C. Hansen, *Rank-deficient and discrete ill-posed problems: numerical aspects of linear inversion,"* Philadelphia: SIAM, 1998.

[15] A. Hinton, M. Perea-Ortiz, J. Winch, J. Briggs, S. Freer, D. Moustoukas, S. Powell-Gill, C. Squire, A. Lamb, C. Rammeloo, B. Stray, G. Voulazeris, L. Zhu, A. Kaushik, Y-H, Lien, A. Niggebaum, A. Rodgers, A. Stabrawa, D. Boddice, S.R. Plant, G. Tuckwell, K. Bongs, N. Metje and M. Holynski, "A portable

magneto-optical trap with prospects for atom interferometry in civil engineering," Phil. Trans. Roy. Soc. A, Math. Phys and Eng. Sci. 375, 2017.

[16] W.J. Hinze, R.R.B. von Frese and A.H. Saad, *Gravity and magnetic exploration: Principles, practices and applications.* Cambridge: Cambridge University Press, 2013.

[17] Y. Li and D.W. Oldenburg, "3D inversion of magnetic data," Geophysics, vol. 61, no. 2, pp. 394-408, March 1996.

[18] Y. Li and D.W. Oldenburg, "3D inversion of gravity data," Geophysics, vol. 63, no. 1, pp. 109-119, Jan. 1998.

[19] F. Moreau, D. Gilbert, M. Holschneider and G. Saracco, "Wavelet analysis of potential fields", *Inverse Problems*, vol. 13, 165-178, 1997.

[20] V. Paoletti, S. Ialongo, G. Florio, M. Fedi and F. Cella, "Self-constrained inversion of potential fields," *Geophys. J. Int.*, vol. 195, pp. 854-869. 2013.

[21] V. Paoletti, P.C. Hansen, M.F. Hansen and M. Fedi, "A computationally efficient tool for assessing the depth resolution in large-scale potential-field inversion," *Geophysics*, vol. 79, no. 4, pp. A33-A38, July 2014.

[22] V. Paoletti, M. Fedi, F. Italiano, G. Florio and S. Ialongo, "Inversion of gravity gradient tensor data: does it provide better resolution?," *Geophys. J. Int.,* vol. 205, no. 1, pp. 192-202, Feb. 2016.

[23] M. Pilkington, "Analysis of gravity gradiometer inverse problems using optimal design measures," *Geophysics,* vol. 77, no. 2, pp. G25-G31, March 2012.

[24] O. Portniaguine and M.S. Zhdanov, "Focusing geophysical inversion images," *Geophysics*, vol. 64, no. 3, pp. 874-887, May 1999.

[25] A.B. Reid, J.M. Allsop, H. Granser, A.J. Millett and I.W. Somerton, "Magnetic interpretation in three dimensions using Euler deconvolution", *Geophysics*, vol. 55, 80-91, 1990.

[26] L. Rossi, *Bayesian interpretation of gravity data with geological prior information*, PhD thesis, Politecnico di Milano. 2013.

[27] A. Roy, "Ambiguity in geophysical interpretation," *Geophysics*, vol. 27, no. 1, pp. 90–99, Feb. 1962.

[28] J. B. C. Silva, W. E. Medeiros, and V. C. F. Barbosa, "Potential field inversion: Choosing the appropriate technique to solve a geologic problem," *Geophysics*, vol. 66, no. 2, pp. 511–520, March 2001.

[29] D.C. Skeels, "Ambiguity in gravity interpretation," *Geophysics*, vol. 12, no.1, pp. 43-56, Jan. 1947.

[30] R.A. Smith and M.H.P. Bott, "The estimation of limiting depth of gravitating bodies", *Geophys. Prosp.* vol.6, 1-10. 1958.

[31] R.A. Smith, "Some depth formulae for local magnetic and gravity anomalies", *Geophys.Prosp.* vol.7, 55-63. 1959.

[32] F. Sorrentino, Q. Bodart, L. Cacciapuoti, Y.-H. Lien, M. Prevedelli, G. Rosi, L. Salvi, and G. M. Tino, "Sensitivity limits of a Raman atom interferometer as a gravity gradiometer," *Phys. Rev. A*, vol. 89, p. 023607, Feb. 2014.

[33] G.W. Stewart, *Introduction to matrix computations.* Orlando: Academic Press, 1973.

[34] M.S. Zhdanov, *Geophysical inverse theory and regularization problems*, Elsevier Science, 2002.

[35] M.S. Zhdanov, *Inverse theory and applications in geophysics, 2nd edition.* Amsterdam: Elsevier. 2015.

[36] M.S. Zhdanov, X. Liu and G. Wilson, "Potential field migration for rapid 3D imaging entire gravity gradiometry surveys", First Break, vol. 28, 47-51, 2010.